Title

Quantitative accuracy in total-body imaging using the uEXPLORER PET/CT scanner

Journal

Physics in Medicine and Biology, 66(20)

ISSN

0031-9155

Authors

Leung, Edwin K

Berg, Eric

Omidvari, Negar

et al.

Publication Date

2021-10-21

DOI

10.1088/1361-6560/ac287c

Peer reviewed

HHS Public Access

Author manuscript

Phys Med Biol. Author manuscript; available in PMC 2022 October 11.

Published in final edited form as:

Phys Med Biol. ; 66(20): . doi:10.1088/1361-6560/ac287c.

Quantitative accuracy in total-body imaging using the uEXPLORER PET/CT scanner

Edwin K. Leung[1,2], **Eric Berg**[2], **Negar Omidvari**[2], **Benjamin A. Spencer**[1], **Elizabeth Li**[2], **Yasser G. Abdelhafez**[1], **Jeffrey P. Schmall**[3], **Weiping Liu**[4], **Liuchun He**[4], **Songsong Tang**[4], **Yilin Liu**[4], **Yun Dong**[4], **Terry Jones**[1], **Simon R. Cherry**[1,2], **Ramsey D. Badawi**[1,2]

[1]Department of Radiology, UC Davis Health, Sacramento, CA, United States

[2]Department of Biomedical Engineering, University of California, Davis, Davis, CA, United States

[3]UIH America Inc., Houston, TX, United States

[4]Shanghai United Imaging Healthcare Co. Ltd., Shanghai, China

Abstract

Absolute quantification of regional tissue concentration of radioactivity in PET is a critical parameter-of-interest across various clinical and research applications and is affected by a complex interplay of factors including scanner calibration, data corrections, and image reconstruction. The emergence of long AFOV PET systems widens the dynamic range accessible to PET and creates new opportunities in reducing scan time and radiation dose, delayed or low radioactivity imaging, as well as kinetic modeling of the entire human. However, these imaging regimes impose challenging conditions for accurate quantification due to constraints from image reconstruction, low count conditions, as well as large and rapidly changing radioactivity distribution across a large AFOV. We comprehensively evaluated the quantitative accuracy of the uEXPLORER total-body scanner in conditions that encompass existing and potential imaging applications (such as dynamic imaging and ultralow-dose imaging) using a set of total-body specific phantom and human measurements. Through these evaluations we demonstrated a relative count rate accuracy of ± 3 – 4% using the NEMA NU 2–2018 protocol, an axial uniformity spread of ± 3% across the central 90% AFOV, and a 3% activity bias spread from 17 – 474 MBq ^{18}F-FDG in a 210 cm-long cylindrical phantom. Region-of-interest quantification spread of 1% was found by simultaneously scanning three NEMA NU 2 image quality phantoms, as well as relatively stable volume-of-interest quantification across 0.2 – 100% of total counts through re-sampled datasets. In addition, an activity bias spread of −2% to +1% post-bolus injections in human subjects was found. Larger bias changes during the bolus injection phase in humans indicated the difficulty in providing accurate PET data corrections for complex activity distributions across a large dynamic range. Our results overall indicated that the quantitative performance achieved with the uEXPLORER scanner was uniform across the AFOV and provided the accuracy necessary to support a wide range of imaging applications.

Introduction

Absolute quantification of regional tissue concentration of radioactivity is a hallmark of positron emission tomography (PET), and the quantitative accuracy provided in

the reconstructed images is a critical parameter-of-interest across research and clinical imaging applications. Accurate quantification is essential for kinetic modeling, lesion characterization, and measuring tumor response to therapy (Carson 2003, Wahl 2009). Quantitative accuracy in PET is affected by a complex interplay of factors, from the scanner calibration to the PET data corrections and image reconstruction parameters (Badawi 1999, Brasse 2005, Johansson 2007, van Velden 2009, Lockhart 2011, Walker 2011, Jian 2015), along with application-dependent factors such as total activity, activity distribution, and patient habitus (Boellaard 2009, Boland 2009, El Fakhri 2009).

The emergence of total-body PET imaging with a long axial field-of-view (FOV) system (e.g. 194 cm in the uEXPLORER PET/CT scanner (Spencer 2020)) enables the entire adult human body to be imaged in a single bed position for the first time (Badawi 2019), and provides approximately 40-fold higher sensitivity for whole-body imaging compared to conventional PET systems with 15 – 30 cm axial FOV that comprise the majority of PET systems available for human imaging (Bettinardi 2004, Teräs 2007, Bettinardi 2011, Jakoby 2011, Poon 2012, Miller 2015, Rausch 2019, Van Sluis 2019). The sensitivity gain and the long axial FOV aspect of total-body PET provides increased image signal-to-noise ratio (SNR) and widens the dynamic range accessible to PET, creating new clinical research and healthcare opportunities in: (1) radiation dose reduction (Badawi 2019, Liu 2021), (2) dynamic imaging with short image frame durations (Zhang 2020), (3) delayed or low-activity imaging (Berg 2020, Beckford Vera 2020), and (4) kinetic modeling of the entire human body (Feng 2020, Wang 2020, Zhang 2020).

While these and other imaging regimes are now possible with total-body PET imaging from a signal-to-noise ratio (SNR) standpoint, they introduce challenging conditions for accurate quantification. For example, the non-linearity and non-negativity constraints imposed by iterative image reconstruction makes quantification challenging when there are few coincidence events contained in the image (e.g. in low-dose, short frame durations, and delayed imaging). In addition, variations in count rates and scatter fraction across the long axial FOV may be large and rapidly changing in some imaging applications, particularly in the early phase of total-body dynamic acquisitions. The scanner also has approximately an order of magnitude greater volume of scintillator material (Jakoby 2011, Spencer 2020) and, when combined with an increased axial acceptance angle, leads to higher ^{176}Lu background count rate than shorter conventional PET scanners. The ^{176}Lu background (7.5 Mcps singles and 93 – 94 kcps coincidence background rates for the uEXPLORER scanner) will comprise the bulk of the PET data at very low levels of radiotracer activity.

The goal of this work is to evaluate the quantitative accuracy of the uEXPLORER scanner in a variety of conditions that encompass existing and potential foreseen imaging applications, including total-body high-dose dynamic imaging and ultralow-dose imaging within the dynamic ranges as depicted in Figure 1. To that end, we devised a set of total-body specific phantom and human measurements to comprehensively characterize the quantitative accuracy of the uEXPLORER scanner across a wide range of activity and count rate scenarios. These measurements included global quantification bias assessments using an extended NEMA NU 2 scatter phantom and a long uniform water cylinder scanned at various activity levels and scan durations, in addition to the more traditional methods

of evaluating regional bias and variability in regions-of-interest (ROIs) by simultaneously imaging three NEMA image quality (IQ) phantoms.

In addition to phantom evaluations, a set of healthy human studies performed on the uEXPLORER scanner at the EXPLORER Molecular Imaging Center (Sacramento, CA, United States) were used to measure global quantitative bias. Evaluating absolute quantitative accuracy in human subjects is a challenging task due to the absence of ground truth radioactivity concentration in different organs. Furthermore, since conventional PET scanners capture the signal from only a 20 – 30 cm axial region at any time, validating absolute PET quantification relative to the total injected radioactivity in human subjects is difficult and may be prone to error, since there is no direct knowledge of the total radioactivity inside the axial FOV of the scanner. Therefore, the evaluation of quantitative accuracy in PET has, for the most part, been limited to ROI evaluations in short phantoms with known radioactivity concentrations, but which do not represent realistic conditions for human imaging (i.e. with significant variations in attenuation, scattering, and radioactivity distribution). An exception is the work of Lodge 2021, where the accuracy of a conventional PET/CT scanner was assessed in the descending thoracic aorta by means of venous sampling. Here, we make use of the total-body coverage provided by the uEXPLORER scanner's 194 cm axial FOV to evaluate absolute quantitative accuracy in human dynamic imaging studies for the first time, since all the radioactivity is always confined within the FOV throughout the acquisition shortly after radiotracer injection.

Methods

System parameters

The 194 cm-long uEXPLORER PET/CT scanner consists of 8 PET scanner units, with a ring diameter of 786 mm. There are 24 detector modules in each unit. Each module contains 5 × 14 (transaxial × axial) detector blocks, where each block contains 7 × 6 (transaxial × axial) scintillator crystals (each 2.76 × 2.76 × 18.1 mm^3). The time-of-flight (TOF) resolution of the system is 505 ps, and the spatial resolution of the system is ≤ 3.0 mm full width at half maximum (FWHM) near the center of the axial FOV. The system utilizes a scanner unit-based variable time window (4.5 – 6.9 ns) and allows each unit to form coincidence events with up to a maximum unit difference of 4, which corresponds to a maximum axial acceptance angle of 57.0°. The energy window is 430 – 645 keV. Additional information regarding the system performance is available in Spencer 2020.

Image reconstruction

The PET images were reconstructed in a research-only environment, using the vendor-provided list-mode time-of-flight, ordered-subset expectation-maximization (TOF-OSEM) reconstruction platform (a clinical release R001.2-based, stand-alone hardware and software environment extended with customizable offline reconstruction and other research functionality) installed on in-house computational hardware. In this software environment we were given direct access to all intermediate reconstruction files and PET data correction files (e.g. normalization and dead-time lookup tables (LUTs)). This enabled us to investigate the effects from changes made into individual correction files on the quantification accuracy

of the reconstructed images without making changes to the underlying reconstruction and data correction algorithms. As a result of this investigation, updated normalization and dead-time LUTs provided by the vendor were used for this work. All results presented in this paper used the same data correction parameters and these parameters were not fine-tuned for individual studies. To maximize computational efficiency and to minimize effects from varying reconstruction parameters, only one set of reconstruction parameters was employed for all experiments: All images were reconstructed with 4 iterations, 20 subsets, and with 4 mm isotropic voxels in a 150 × 150 × 486 image matrix. Resolution modeling (i.e. point spread function (PSF)) was not included, and no post-reconstruction smoothing was applied to the images. All other PET data corrections were applied throughout the studies, including corrections for scatter and random coincidences, attenuation, deadtime, normalization, and radioactive decay. Random coincidences were estimated for each block-pair using a delayed coincidence channel. Scattered coincidences were estimated for each dual-block (7 transaxial × 12 axial crystals) pair using Monte Carlo simulations independently for each image frame. Dead-time correction was performed using a non-paralyzable model with block singles rates from a high-count scan of an acrylic uniform water cylinder (16.5 cm outer diameter, 15 cm inner diameter, 210 cm long) filled with approximately 500 MBq of ^{18}F-FDG at the start of the scan. Attenuation correction factors (ACFs) were obtained from a low-dose co-registered CT image acquired for each imaging study. Prior to calculating ACFs, the CT images were pre-processed using a custom patch to remove artifacts that manifested at the edge of the FOV, which were found to introduce bias. These low-intensity artifacts were present in the form of an annulus with an internal diameter of 500 mm and extending to 700-mm diameter transaxial CT FOV and the extent of their effect on the bias depended on the size of the object and its position relative to the CT FOV. The scanner manufacturer has implemented a fix that will be released in the next version of the clinical software. Normalization factors (crystal efficiency and plane efficiency) were obtained with a 20 cm diameter × 30 cm long ^{68}Ge uniform cylinder that was stepped over the axial FOV for a total time of 45 min. The reconstruction quantification factor (QF) used for absolute quantification was obtained with a 20 cm diameter × 30 cm long ^{18}F-FDG uniform cylinder positioned at the center of the scanner. The dose calibrator (Capintec CRC-55tR) used for the study was calibrated daily in accordance with the recommended calibration procedure from the owner's manual.

Accuracy of count rate corrections

The 70-cm NEMA NU 2 scatter phantom and a 175-cm extended version of it were used to evaluate count-rate dependent quantitative accuracy. The standard 70-cm phantom was assembled using four 17.5 cm polyethylene phantom sections, while the extended phantom consisted of ten sections. Each phantom was positioned at the center of the scanner, and a decay series of acquisitions over 10 h were acquired for each phantom. Initial ^{18}F-FDG activities were 370 MBq for the 70 cm phantom, and 441 MBq for the 175 cm phantom. Both experiments were acquired until the activity reached < 10 MBq. The NEMA NU 2–2018 accuracy test was performed for both the standard 70 cm phantom using image slices within the central 65 cm of the axial FOV, and the central 170 cm axial FOV for the 175 cm phantom. The quantitative accuracy was assessed based on the relative percent trues error.

Uniform phantom

An acrylic uniform water cylinder (16.5 cm outer diameter, 15 cm inner diameter, 210 cm long) was filled with ^{18}F-FDG and was positioned at the center of the scanner. List-mode data were acquired at five time points over 10 h, from 474 MBq to 17 MBq in the FOV of the scanner. The scan duration for each acquisition was 60 min, and a series of 5-min dynamic PET images (12 time frames total) were reconstructed. Axial uniformity was evaluated with this phantom based on the normalized mean values for each slice within a concentric 130-mm diameter circular ROI, using the 0 – 5 min image from each of the five datasets. The global activity-dependent bias was evaluated by comparing the activity sum in the image to the known activity in the axial FOV of the scanner with dynamic (5-min × 12 time frames) reconstructed images.

Regional bias and variability

The triple NEMA IQ phantom evaluation was based on the NEMA NU 2–2018 IQ assessment (4:1 hot-to-warm background concentration). In this modified protocol, 3 IQ phantoms and a NU 2 scatter phantom were filled according to the NEMA protocol and were positioned as shown in Figure 2, with the third IQ phantom abutting the NU 2 scatter phantom (IQ #3) and positioned near the center of the scanner. To yield constant activity concentrations in the three IQ phantoms, a single radiotracer dose diluted in a one-liter saline bag was used to fill all the hot spheres and another single radiotracer dose diluted in 33.4 L of water was used to fill the background volume in all three phantoms. Given the small variations in total volume of the three phantoms, this resulted in a total activity of 42.9, 42.7, and 43.4 MBq in IQ #1, #2, and #3, respectively. Data were acquired over 12 h, with six 1-hour data acquisitions, from 217 MBq to 2 MBq of ^{18}F-FDG in the FOV of the scanner. An ROI-based analysis was performed by assessing the bias of the warm background of each IQ phantom using 30-min static reconstructions. On every slice of the central 10 cm axial length of the phantom (27 slices), twelve circular ROIs (37 mm diameter) were drawn on the warm background region of each IQ phantom (Spencer 2020) – fulfilling the NEMA NU 2–2018 background ROI placement criteria – to evaluate the quantitative bias of the ROIs relative to the known warm background activity concentration.

Also, to assess the effect of total counts on the bias and noise of the reconstructed images, 30-mm diameter spherical volumes-of-interest (VOIs) were drawn on the 37 mm hot sphere and warm background of each IQ phantom. The VOI for the warm background was placed in proximity of the 28-mm and 37-mm-diameter spheres, at approximately 107 mm radial offset from the center. Two types of images were used for this analysis: (1) 30-min static images at each time point, and (2) re-sampling of 60-min data (and portions of it) into 30 dynamic images that contained equivalent number of counts in each time frame, similar to the re-sampling strategy described in Jian 2015.

Dynamic quantification in humans

Dynamic images from two representative human research scans injected with ^{18}F-FDG were used to evaluate the global quantitative accuracy in human subjects over the scan duration at two activity levels: 370 MBq (80.8 kg, 165.1 cm) and 21 MBq (84.4 kg, 170 cm) injected activity. The studies were IRB-approved (#1341792), and the subjects provided informed

consent. The subjects were placed in a supine position with their hands to the side. Data acquisition began immediately with radiotracer injection in the antecubital vein. The scan duration was 60 min. For this evaluation, a dynamic reconstruction framing protocol that consists of 66 frames (30 × 2 s, 12 × 10 s, 6 × 30 s, 12 × 120 s, and 6 × 300 s) was used. Since the injected activities were completely within the FOV, the global activity bias was evaluated by computing the percent bias of the activity sum in a total-body ROI to the known injected radiotracer activity.

Results

Count rate dependent quantitative accuracy

Figures 3 and 4 show the relative percent trues error of the standard 70 cm and extended 175 cm NU 2 scatter phantoms, plotted against activity concentration, as well as the average activity in the phantom (located on the top x-axis), respectively. The mean relative trues errors for both phantoms ranged between ±3 – 4%, from approximately 10 to 400 MBq.

Uniform phantom

Figure 5 shows the axial uniformity plotted against axial slice position, measured with the uniform phantom at 3 radioactivity levels, from 17 MBq to 474 MBq. The uniformity spread was ± 3% in the central 90% axial FOV of the scanner. The normalized root-mean-square errors (NRMSE) of the central 90% of the slices were 1.7% (17 MBq), 1.3% (151 MBq), and 1.2% (474MBq). Figure 6 shows the global activity bias of the uniform phantom, plotted against the activity in the FOV of the scanner. The bias ranged from 1.3% to 4.3%, from 17 MBq to 474 MBq, respectively.

Triple NEMA IQ phantom

Figure 7 shows the warm background ROI biases of the three IQ phantoms. The mean biases (from the known warm background concentration) of the three IQ phantoms ranged between +4%/+5%, from 22 MBq to 217 MBq. Figure 8 shows the box plots of the VOI biases of the 37 mm hot sphere and the background of the 3rd IQ phantom, with the effective total counts of each image (normalized to the first 30 min of the first scan) shown on the upper x-axis. The biases ranged between −5%/−3% for the hot sphere, and −1/+6% for the background, between 0.2 – 100% of effective counts.

Human subjects

Figure 9 shows the activity bias of the human subjects, with the uniform phantom reconstructed using the same 66-frame dynamic protocol shown as reference. For both human subjects, the bias changed quickly during the initial bolus phase before becoming consistent at ~ 60-s post-injection with approximately −2%/+1% bias in both subjects. For the uniform phantom, the biases ranged between +1%/+4% for the 300-s frames.

Discussion

The quantitative accuracy of the uEXPLORER total-body PET/CT scanner was evaluated for both static and dynamic imaging using phantom and human datasets. Overall, consistent

quantification was obtained throughout most experiments, across a wide range of activity levels, activity distributions, and image frame durations. Except at very low activities (< 25 MBq), the total variation in image bias was < 3% with the 70 cm NEMA NU 2 scatter phantom up to the peak NECR activity. Three general trends were observed in the count rate quantification experiments: (1) negative correlation of relative count rate error with activity, (2) non-linear error at low ^{18}F-FDG activities (< 25 MBq), and (3) a transition point in error at approximately 25 MBq that is more pronounced in the 175 cm extended scatter phantom. Our investigations suggested that the activity-dependent count rate error may be related to imperfect background subtraction from the substantial presence of ^{176}Lu background in the LYSO crystals. The transition in error observed at ~ 25 MBq with the scatter phantoms may also be related to the total number of counts in each acquisition: to obtain sufficient temporal sampling at low activity datapoints, the acquisition times were reduced, which means even fewer counts were acquired at the low activity region. Previous literature has suggested that the number of counts in a PET acquisition may lead to biases in images reconstructed using OSEM (Johansson 2007, van Velden 2009, Walker 2011, Jian 2015). Another possible cause may be inaccuracies due to the use of single-precision floating point calculation. These effects in total-body PET will be investigated in greater detail in future experiments. Early data from the manufacturer suggests that using double-precision floating point calculation and a reduced number of subsets in the reconstruction may result in improved accuracy at activities below ~25 MBq. For example, the average bias of the 30 frames for the first 60s of the uniform phantom (17 MBq) scan reconstructed with 8 iterations and 10 subsets improved from −5% to +2.5%.

Uniformity assessment performed on the 2 m-long cylinder phantom data showed up to ±3% variations across the central 90% axial FOV. The patterns in axial uniformity were largely conserved across the range of activity investigated and were correlated with the normalization plane efficiency factors. The non-uniformities may be caused by using a shorter uniform cylinder (20 cm-diameter × 30 cm-long) that was stepped through the axial FOV for normalization calibration compared to the 2 m-long uniform cylinder used for this assessment and suggests that modifications to the algorithm used for estimating the normalization factors may be appropriate. For instance, inaccuracies in normalization factor estimations for the more oblique LORs may result in bias propagation and non-uniformities across the axial FOV, in addition to differences in attenuation and scatter between the two phantoms that is typically not a consideration in PET normalization when using a shorter phantom with less attenuation. However, the use of a 2 m-long phantom is challenging in practice, largely due to its size and weight in addition to potential imperfect mixing of the radionuclide.

Quantitative biases in each of the three IQ phantoms in the triple IQ experiment were stable above ~ 25 MBq and further demonstrates accurate and axially uniform quantification with a non-uniform radioactivity distribution. The decrease in bias at the low end of the activity may be attributed to the compounding effects of low total number of counts and a high number of subsets used in the OSEM reconstruction. Also, the total activity in the FOV at the end was only 2 MBq and may be similarly responsible for the large standard deviation observed in these datapoints. In the future, a detailed assessment using various

reconstruction parameters and with varying number of iterations and subsets may further help evaluate the quantitative accuracy in total-body PET across a wide dynamic range.

For dynamic imaging, 3% variations in quantification biases were observed in both phantoms and humans, except with short frame durations (< 5 s). In humans, the changing activity distribution is a confounding factor in determining the root cause of activity bias, but not in the phantom. Thus, based on the phantom results, the changes in bias that occur when the frame length changes may be due to differences in the total number of counts in the image, which may impact scatter estimation. In the human subject assessment, four out of six data points in the 300-s frames of the 21 MBq human subject showed a positive bias. We note that this may be attributed to the scatter correction since the scatter fractions reported in the DICOM headers were slightly lower for those image frames compared to other 300-s frames. While the bias in the human scans did not seem to be dependent on the injected activity in the latter half of the 60-min scan, caution should be exercised to not overinterpret the results. Other complex, physiologic factors specific to human data may easily come into play, such as voluntary and involuntary motion that results in misalignment between the PET and CT images, and the initially rapid, time-varying activity distribution following the bolus injection, all of which may lead to biases that may have compounding or opposing effects. Also, each patient has a unique body habitus and activity distribution that are distinct from each other, as well as from the shape and distribution of the uniform phantom. Utilization of an image-derived input function (IDIF) for dynamic PET kinetic modeling may mitigate the effects of the larger biases present in the shorter frames; since scatter correction is applied on a per frame basis, both the IDIF and tissue of interest may be similarly affected. The opposing effects in bias changes with short frame durations between high and low activities is peculiar, and possibly related to the frame-based scatter estimation and/or the effect of random coincidences from ^{176}Lu background events that comprise most of the singles and prompt coincidences at low activity. The TOF image reconstruction with approximately 500 ps FWHM resolution and a 430 keV lower energy threshold would adequately remove any true coincidences formed from the ^{176}Lu beta decay and the 307 keV gamma emissions from the total-body ROIs. However, the background singles subtraction performed during deadtime correction is subject to drift in the detectors and therefore may impact quantification at very low activities. These are all a subject for future investigations. The small positive bias of the uniform phantom with high activity may be attributed to count-rate dependent variations in the energy and/or TOF calibrations, in addition to the different object geometry compared to that used for scanner calibration, which further demonstrates the need for highly accurate physics corrections.

As mentioned earlier, one of the greatest challenges in PET quantification is that the quantitative accuracy is impacted by a complex interplay of multiple physical factors, along with the exact implementation of scanner calibrations, data corrections and image reconstruction parameters, many of which are proprietary and specific to the scanner manufacturer. A comprehensive quantitative study using an independent reconstruction platform may be beneficial to completely understand the origin of all types of biases observed, however this is beyond the scope of this study. Two primary types of biases were observed in the study: (1) bias that depends on the amount of radioactivity in the FOV; and (2) bias that depends on the number of total counts in the image. Based on

our results, quantification in dynamic imaging studies may be most impacted by the frame length-dependent biases. Clinical and research imaging studies with total-body PET, both high and low dose, with static image reconstruction and long frame durations (i.e. > 30 s) are expected to exhibit quantification bias within ± 5%.

Conclusion

The quantitative imaging accuracy of the first total-body PET imaging system, the uEXPLORER PET/CT scanner, was evaluated using a set of experiments devised to cover the range of activity and count rates representative of clinical and research total-body imaging applications. Through these evaluations we demonstrated a relative count rate quantification accuracy of ± 3 – 4%, an axial uniformity spread of ± 3% across the central 90% axial FOV (175 cm region), and a 3% activity bias from low to high activity (17 – 474 MBq) in a 2 m-long uniform phantom. We also showed a stable ROI quantification of 1% from 22 – 217 MBq with the triple IQ phantoms, and relatively stable VOI quantification across 0.2 – 100% of total counts through re-sampled datasets. In addition, we showed an activity bias spread of −2% to +1% post-bolus injections in human subjects in the 2 – 5 min frames. Larger bias changes during the bolus injection phase in humans indicated the difficulty in providing accurate PET data corrections for complex activity distribution across a very large dynamic range. While there are opportunities to optimize the data corrections and image reconstruction parameters, our results overall indicate that the quantitative performance achieved with the uEXPLORER total-body PET/CT scanner is uniform across the axial FOV and provides the accuracy necessary to support a wide range of imaging applications spanning from low-dose studies to dynamic imaging with commonly used frame lengths.

Acknowledgement

Funding sources for this work include NIH R01 CA249422 and NIH R01 CA206187.

Disclosure

UC Davis has a research agreement and a sales-based revenue sharing agreement with United Imaging Healthcare. Ramsey D. Badawi and Simon R. Cherry are principal investigators on a research grant funded by United Imaging Healthcare.

References

Badawi RD and Marsden PK (1999). “Developments in component-based normalization for 3D PET.” Physics in Medicine and Biology 44(2): 571–594. [PubMed: 10070802]

Badawi RD, Shi HC, Hu PC, Chen SG, Xu TY, Price PM, Ding Y, Spencer BA, Nardo L, Liu WP, Bao J, Jones T, Li HD and Cherry SR (2019). “First Human Imaging Studies with the EXPLORER Total-Body PET Scanner.” Journal of Nuclear Medicine 60(3): 299–303. [PubMed: 30733314]

Berg E, Gill H, Marik J, Ogasawara A, Williams S, van Dongen G, Vugts D, Cherry SR and Tarantal AF (2020). “Total-Body PET and Highly Stable Chelators Together Enable Meaningful Zr-89-Antibody PET Studies up to 30 Days After Injection.” Journal of Nuclear Medicine 61(3): 453–460. [PubMed: 31562219]

Bettinardi V, Danna M, Savi A, Lecchi M, Castiglioni I, Gilardi MC, Bammer H, Lucignani G and Fazio F (2004). “Performance evaluation of the new whole-body PET/CT scanner: Discovery ST.” European Journal of Nuclear Medicine and Molecular Imaging 31(6): 867–881. [PubMed: 14770270]

Bettinardi V, Presotto L, Rapisarda E, Picchio M, Gianolli L and Gilardi MC (2011). "Physical Performance of the new hybrid PET/CT Discovery-690." Medical Physics 38(10): 5394–5411. [PubMed: 21992359]

Boellaard R (2009). "Standards for PET Image Acquisition and Quantitative Data Analysis." Journal of Nuclear Medicine 50: 11S–20S. [PubMed: 19380405]

Boland GWL, Blake MA, Holalkere NS and Hahn PF (2009). "PET/CT for the Characterization of Adrenal Masses in Patients with Cancer: Qualitative Versus Quantitative Accuracy in 150 Consecutive Patients." American Journal of Roentgenology 192(4): 956–962. [PubMed: 19304700]

Brasse D, Kinahan PE, Lartizien C, Comtat C, Casey M and Michel C (2005). "Correction methods for random coincidences in fully 3D whole-body PET: Impact on data and image quality." Journal of Nuclear Medicine 46(5): 859–867. [PubMed: 15872361]

Carson RE (2005). "Tracer Kinetic Modeling in PET." In: Bailey DL, Townsend DW, Valk PE, Maisey MN (eds) Positron Emission Tomography. Springer, London. 10.1007/1-84628-007-9_6

El Fakhri G, Kardan A, Sitek A, Dorbala S, Abi-Hatem N, Lahoud Y, Fischman A, Coughlan M, Yasuda T and Di Carli MF (2009). "Reproducibility and Accuracy of Quantitative Myocardial Blood Flow Assessment with Rb-82 PET: Comparison with N-13-Ammonia PET." Journal of Nuclear Medicine 50(7): 1062–1071. [PubMed: 19525467]

Feng T, Zhao Y, Shi H, Li H, Zhang X, Wang G, Badawi RD, Price PM, Jones T and Cherry SR. Total-Body Quantitative Parametric Imaging of Early Kinetics of FDG J Nucl Med. epub ahead of print; doi:10.2967/jnumed.119.238113

Jakoby BW, Bercier Y, Conti M, Casey ME, Bendriem B and Townsend DW (2011). "Physical and clinical performance of the mCT time-of-flight PET/CT scanner." Physics in Medicine and Biology 56(8): 2375–2389. [PubMed: 21427485]

Jian Y, Planeta B and Carson RE (2015). "Evaluation of bias and variance in low-count OSEM list mode reconstruction." Physics in Medicine and Biology 60(1): 15–29. [PubMed: 25479254]

Johansson J, Clikonen V, Teraes M and Ieee (2007). Quantitative brain imaging using the new, fast iterative histogram-mode reconstruction for the HRRT PET scanner. IEEE Nuclear Science Symposium/Medical Imaging Conference, Honolulu, HI.

Leung EK et al. (2020). "Evaluation of quantitative accuracy in total-body PET." IEEE MIC (M-16–06).

Liu G, Hu P, Yu H et al. (2021). "Ultra-low-activity total-body dynamic PET imaging allows equal performance to full-activity PET imaging for investigating kinetic metrics of ^{18}F-FDG in healthy volunteers." Eur J Nucl Med Mol Imaging 10.1007/s00259-020-05173-3

Lockhart CM, MacDonald LR, Alessio AM, McDougald WA, Doot RK and Kinahan PE (2011). "Quantifying and Reducing the Effect of Calibration Error on Variability of PET/CT Standardized Uptake Value Measurements." Journal of Nuclear Medicine 52(2): 218–224. [PubMed: 21233174]

Lodge MA, Lesniak W, Gorin MA, Pienta KJ, Rowe SP and Pomper MG (2021) Journal of Nuclear Medicine 62 (5): 732–737. [PubMed: 33037089]

Miller M, Zhang J, Binzel K, Griesmer J, Laurence T, Narayanan M, Natarajamani D, Wang S and Knopp M (2015). "Characterization of the Vereos Digital Photon Counting PET System." Journal of Nuclear Medicine 56(3).

Poon JK, Dahlbom ML, Moses W, Balakrishnan K, Wang WL, Cherry SR and Badawi RD (2012). "Optimal whole-body PET scanner configurations for different volumes of LSO scintillator: a simulation study (vol 57, pg 4077, 2012)." Physics in Medicine and Biology 57(23): 8117–8117.

Rausch I, Ruiz A, Valverde-Pascual I, Cal-Gonzalez J, Beyer T and Carrio I (2019). "Performance Evaluation of the Vereos PET/CT System According to the NEMA NU2–2012 Standard." Journal of Nuclear Medicine 60(4): 561–567. [PubMed: 30361382]

Spencer BA, Berg E, Schmall JP, Omidvari N, Leung EK, Abdelhafez YG, Tang S, Deng Z, Dong Y, Lv Y, Bao J, Liu W, Li H, Jones T, Badawi RD and Cherry SR (2020). "Performance evaluation of the uEXPLORER Total-body PET/CT scanner based on NEMA NU 2–2018 with additional tests to characterize long axial field-of-view PET scanners." J Nucl Med. 2021;62:861–870. [PubMed: 33008932]

Teras M, Tolvanen T, Johansson JJ, Williams JJ and Knuuti J (2007). "Performance of the new generation of whole-body PET/CT scanners: Discovery STE and discovery VCT." European Journal of Nuclear Medicine and Molecular Imaging 34(10): 1683–1692. [PubMed: 17661031]

van Sluis J, de Jong J, Schaar J, Noordzij W, van Snick P, Dierckx R, Borra R, Willemsen A and Boellaard R (2019). "Performance Characteristics of the Digital Biograph Vision PET/CT System." Journal of Nuclear Medicine 60(7): 1031–1036. [PubMed: 30630944]

van Velden FHP, Kloet RW, van Berckel BNM, Lammertsma AA and Boellaard R (2009). "Accuracy of 3-Dimensional Reconstruction Algorithms for the High-Resolution Research Tomograph." Journal of Nuclear Medicine 50(1): 72–80. [PubMed: 19091902]

Vera DB, Schulte B, Henrich T, Flavell R, Seo Y, Abdelhafez Y, Badawi R, Cherry S and VanBrocklin H (2020). "First-in-human total-body PET imaging of HIV with Zr-89-VRC01 on the EXPLORER." Journal of Nuclear Medicine 61.

Wahl RL, Jacene H, Kasamon Y and Lodge MA (2009). "From RECIST to PERCIST: Evolving Considerations for PET Response Criteria in Solid Tumors." Journal of Nuclear Medicine 50: 122S–150S. [PubMed: 19403881]

Walker MD, Asselin MC, Julyan PJ, Feldmann M, Talbot PS, Jones T and Matthews JC (2011). "Bias in iterative reconstruction of low-statistics PET data: benefits of a resolution model." Physics in Medicine and Biology 56(4): 931–949. [PubMed: 21248391]

Wang GB, Parikh M, Nardo L, Zuo Y, Abdelhafez Y, Qi JY, Jones T, Price P, Cherry S, Pan CX and Badawi R (2020). "Total-Body Dynamic PET of Metastatic Cancer: First Patient Results." Journal of Nuclear Medicine 61.

Zhang XZ, Cherry SR, Xie ZH, Shi HC, Badawi RD and Qi JY (2020). "Subsecond total-body imaging using ultrasensitive positron emission tomography." Proceedings of the National Academy of Sciences of the United States of America 117(5): 2265–2267. [PubMed: 31964808]

Zhang X, Xie Z, Berg E, Judenhofer MS, Liu W, Xu T, Ding Y, Lv Y, Dong Y, Deng Z, Tang S, Shi H, Hu P, Chen S, Bao J, Li H, Zhou J, Wang G, Cherry SR, Badawi RD and Qi J. Total-Body Dynamic Reconstruction and Parametric Imaging on the uEXPLORER. J. Nucl. Med. 2020 61(2): 285–291. PMID: 31302637 DOI: 10.2967/jnumed.119.230565 [PubMed: 31302637]

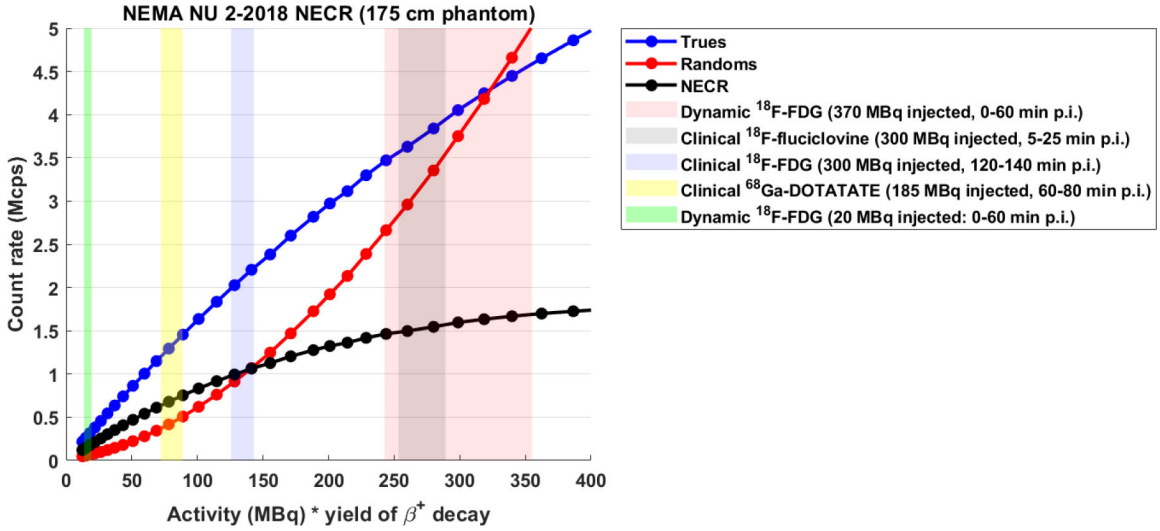

Figure 1.

Range of count rates encountered by the uEXPLORER scanner (throughout the acquisition) in various clinical and research tasks. The count rates were estimated based on the NEMA NU 2–2018 NECR performance assessment using an extended, 175-cm NU 2 scatter phantom (Leung 2020). Note: the activity at peak NECR is 528 MBq, and "p.i." stands for post-injection.

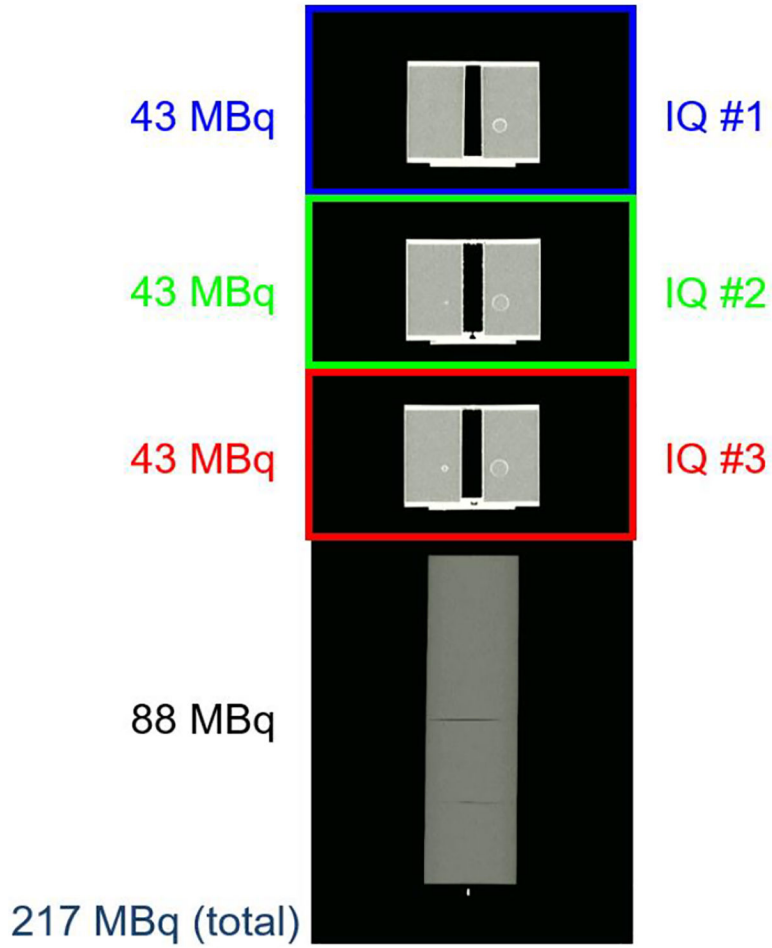

Figure 2.
Position and activity of each phantom in the triple NEMA IQ phantom evaluation.

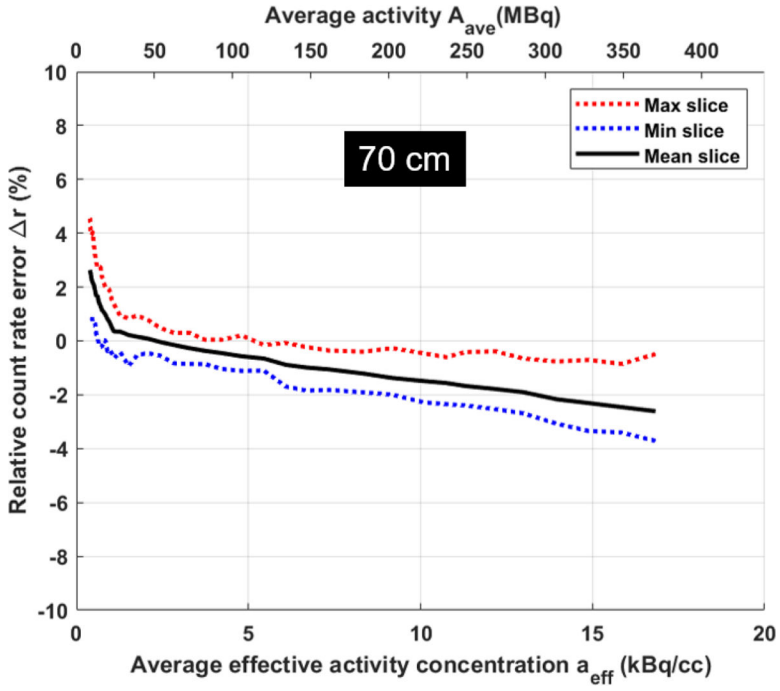

Figure 3.
The relative trues error of the standard 70 cm NU 2 scatter phantom.

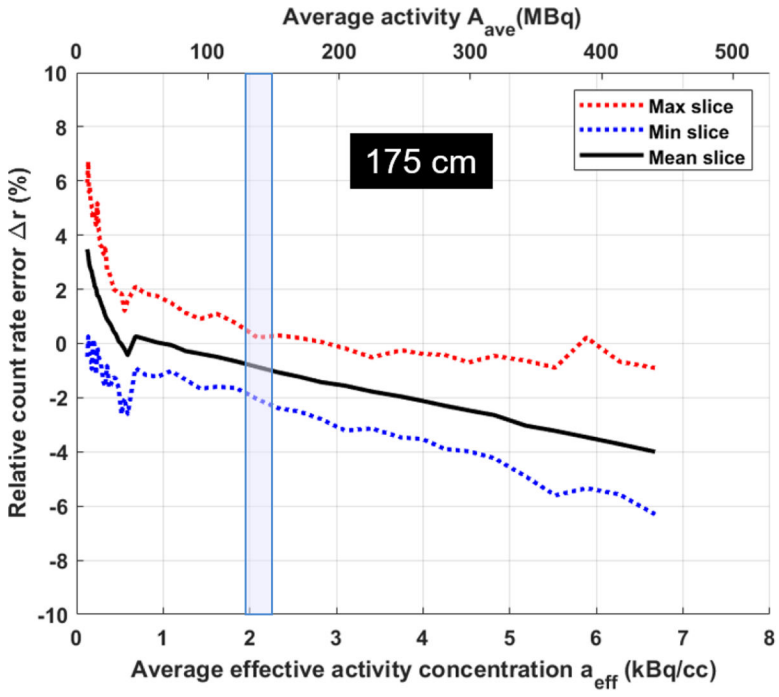

Figure 4.

The relative trues error of the extended 175 cm NU 2 scatter phantom. The shaded blue region represents the average activity throughout an uEXPLORER clinical ^{18}F-FDG scan (~300 MBq injected; scan begins at 120-min post-injection).

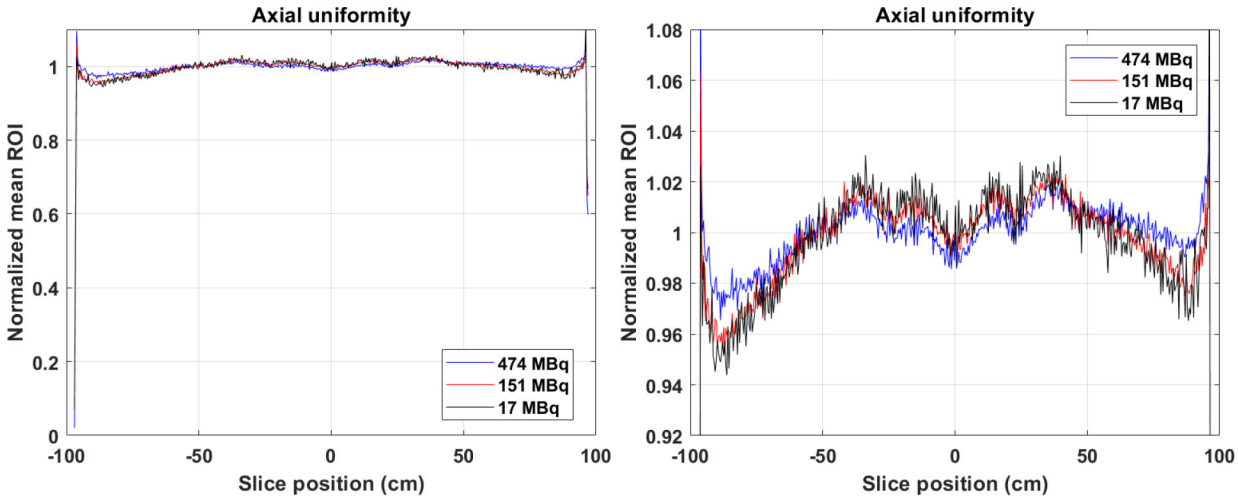

Figure 5.

Axial uniformity of the uEXPLORER scanner. (Left) The y-axis ranged from 0 to 1.1. (Right) The y-axis ranged from 0.92 to 1.08. The normalization factor was based on the ROI average of the central 90% slices.

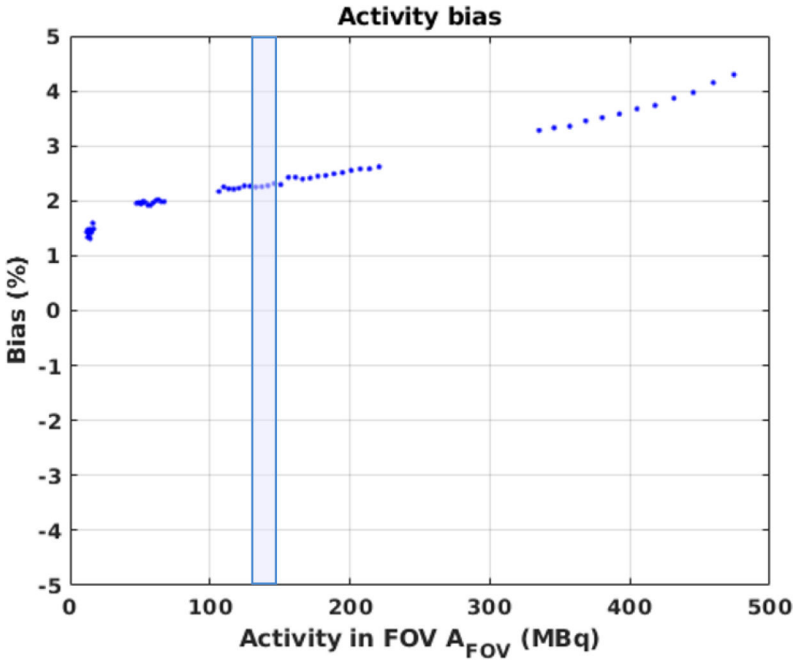

Figure 6.

The global activity bias of the uniform phantom. The shaded blue region corresponds to the average activity throughout an uEXPLORER clinical ^{18}F-FDG scan (~300 MBq injected; scan begins at 120-min post-injection).

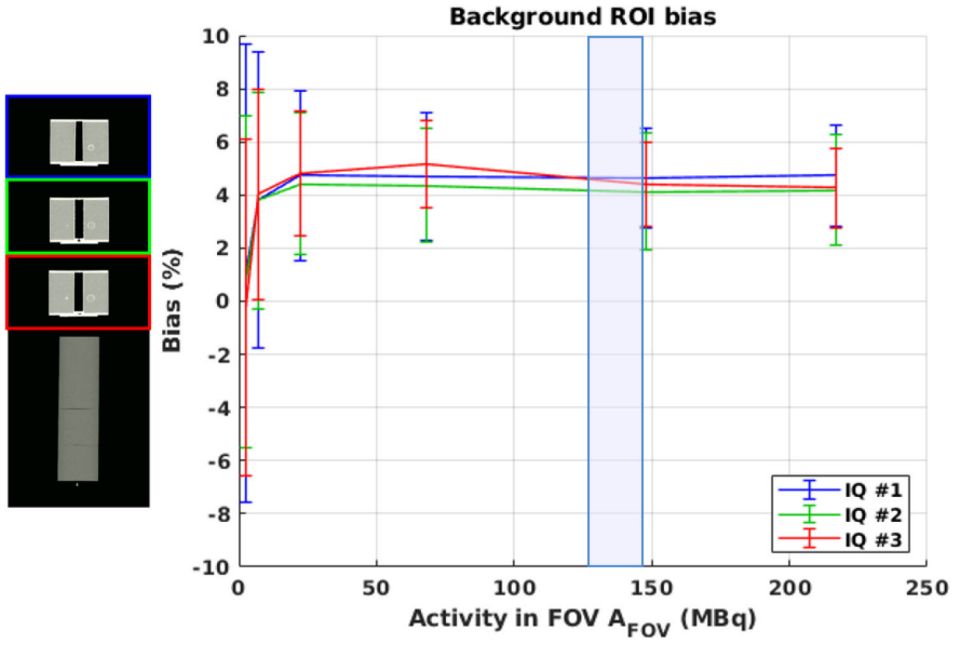

Figure 7.

Bias (mean±SD) of the background ROIs in the 3 IQ phantoms. The error bars indicate the standard deviation (SD) of the mean bias of the 324 background ROIs analyzed for each IQ phantom. The blue shaded region represents the average activity throughout an uEXPLORER clinical ^{18}F-FDG scan (~300 MBq injected; scan begins at 120-min post-injection).

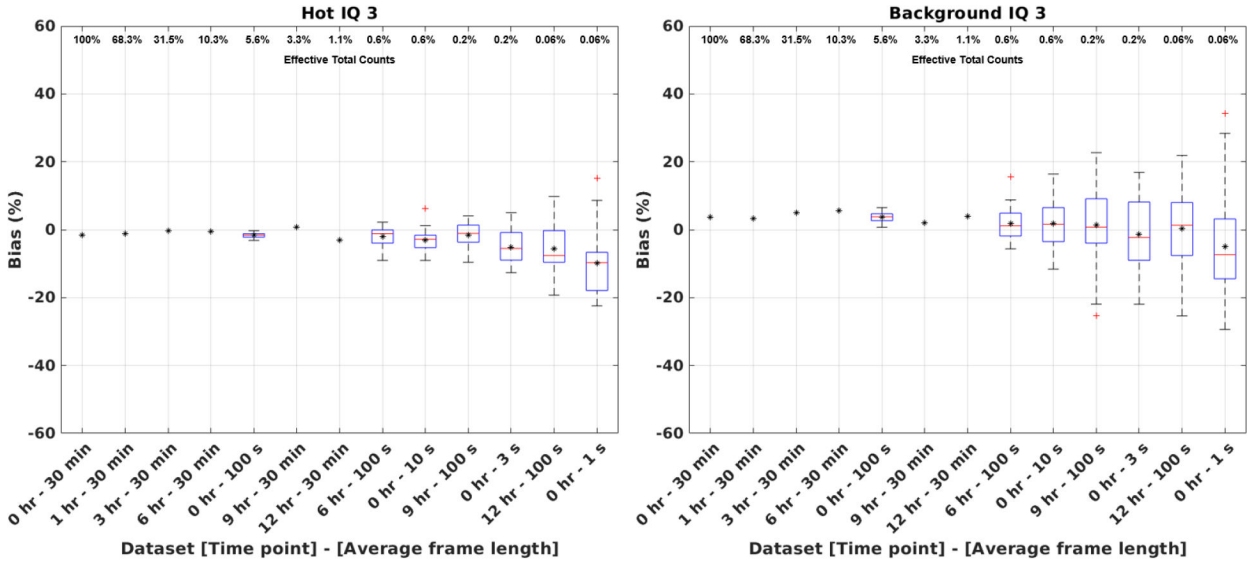

Figure 8.

VOI biases of the (left) 37 mm hot sphere and (right) background of the 3rd IQ phantom. Each label on the x-axis represents the acquisition time point and the average frame duration of the re-sampled dataset, ordered based on the fraction of total counts of the 1st 30-min scan (as shown on the upper x-axis). Mean VOI bias is shown for all datasets using black asterisks. In case of shorter time-frame re-sampled datasets, the mean was calculated on the 30 re-sampled dataset images and box plots were additionally included to display the variations among the 30 datasets.

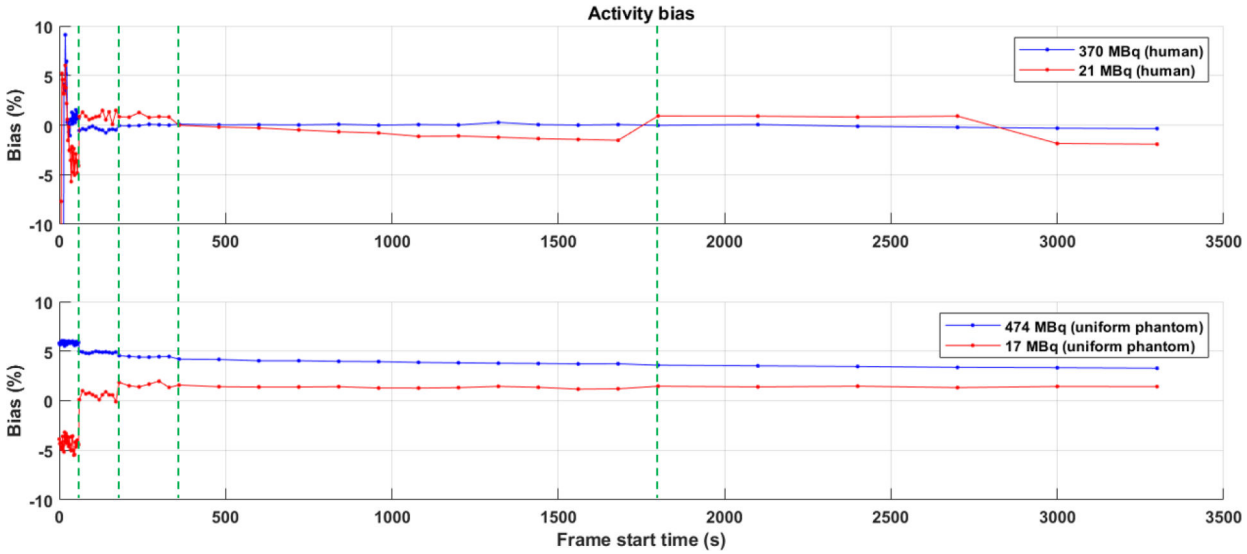

Figure 9.

Activity bias of the (top) human subjects, and (bottom) uniform phantom using the 66-frame reconstruction framing protocol. The vertical dashed lines correspond to the time points where the frame duration changed.